NSTX-U THEORY, MODELING AND ANALYSIS RESULTS

W. GUTTENFELDER[1], D.J. BATTAGLIA[1], E. BELOVA[1], N. BERTELLI[1], M.D. BOYER[1], C.S. CHANG[1], A. DIALLO[1], V.N. DUARTE[1], F. EBRAHIMI[1], E. EMDEE[1], N. FERRARO[1], E. FREDRICKSON[1], N. GORELENKOV[1], W. HEIDBRINK[2], Z. ILHAN[3], S.M. KAYE[1], E.-H. KIM[1], A. KLEINER[1], F. LAGGNER[1], M. LAMPERT[1], J. LESTZ[2], C. LIU[1], D. LIU[2], T. LOOBY[4], N. MANDELL[1], J. MYRA[5], S. MUNARETTO[1], M. PODESTÀ[1], T. RAFIQ[3], Y. REN[1], J. RUIZ-RUIZ[6], F. SCOTTI[7], S. SHIRAIWA[1], V. SOUKHANOVSKII[7], P. VAIL[3], W. WEHNER[3], A. WHITE[8], R. WHITE[1], J. YANG[1], S.J. ZWEBEN[1], S. BANERJEE[9], R. BARCHFELD[10], R.E. BELL[1], J.W. BERKERY[11], A. BHATTACHARJEE[1], G. CANAL[12], X. CHEN[8], N. CROCKER[13], C. DOMIER[10], T. EVANS[14], M. FRANCISQUEZ[1], K. GAN[4], S. GERHARDT[1], R. GOLDSTON[1], T. GRAY[15], A. HAKIM[1], G. HAMMETT[1], S. JARDIN[1], R. KAITA[1], B. KOEL[16], E. KOLEMEN[16], S.-H KU[1], S. KUBOTA[13], B.P. LEBLANC[1], F. LEVINTON[17], N. LUHMANN[10], R. LUNSFORD[1], R. MAINGI[1], R. MAQUEDA[18], J.E. MENARD[1], M. ONO[1], J.-K. PARK[1], F. POLI[1], R. RAMAN[19], M. REINKE[20], T. RHODES[13], J. RIQUEZES[11], C. ROWLEY[16], D. RUSSELL[5], S.A. SABBAGH[11], E. SCHUSTER[3], O. SCHMITZ[21], D.R. SMITH[21], D. STOTLER[1], B. STRATTON[1], K. TRITZ[22], W. WANG[1], Z. WANG[1], AND B. WIRTH[4]

1 Princeton Plasma Physics Laboratory, Princeton University, Princeton, NJ 08543, United States of America
2 University of California at Irvine, Irvine, CA, United States of America
3 Lehigh University, Bethlehem, PA, United States of America
4 University of Tennessee, Knoxville, TN, United States of America
5 Lodestar Research Corporation, Boulder, CO, United States of America
6 Oxford University, Oxford, United Kingdom
7 Lawrence Livermore National Laboratory, Livermore, CA, United States of America
8 Plasma Science and Fusion Center, Massachusetts Institute of Technology, Cambridge, MA, United States of America
9 College of William and Mary, Williamsburg VA, United States of America
10 University of California at Davis, Davis, CA, United States of America
11 Columbia University, New York, NY, United States of America
12 Institute of Physics, University of Sao Paolo, Sao Paolo, Brazil
13 University of California at Los Angeles, Los Angeles, CA, United States of America
14 General Atomics, San Diego, CA, United States of America
15 Oak Ridge National Laboratory, Oak Ridge, TN, United States of America
16 Princeton University, Princeton, NJ, United States of America
17 Nova Photonics, Princeton, NJ, United States of America
18 X Science LLC, Plainsboro, NJ, United States of America
19 University of Washington, Seattle, WA, United States of America
20 Commonwealth Fusion Systems, Cambridge MA, United States of America
21 University of Wisconsin, Madison, WI, United States of America
22 Johns Hopkins University, Baltimore, MD, United States of America

e-mail contact of main author: guttenfe@pppl.gov

Abstract

The mission of the spherical tokamak NSTX-U is to advance the physics basis and technical solutions required for optimizing the configuration of next-step tokamak fusion devices, and to use the unique available capabilities to support ITER and other critical fusion development needs. NSTX-U will ultimately operate at up to 2 MA and 1 T for 5 seconds, and has available up to 15 MW of Neutral Beam Injection (NBI) power at different tangency radii and 6 MW of High Harmonic Fast Wave (HHFW) heating. NSTX-U will operate in a regime where electromagnetic instabilities are expected to dominate transport, and beam-heated NSTX-U plasmas will explore energetic particle (EP) parameter space that is relevant for both α-heated conventional and low aspect ratio burning plasmas. NSTX-U will also develop the physics understanding and control tools to ramp-up and sustain high performance fully-noninductive plasmas, and can generate high target heat fluxes to test conventional and innovative plasma exhaust and PFC solutions. During the period of the NSTX-U Recovery Project (now in the construction and installation phase), there has been considerable analysis, theory and modelling progress in the areas of core MHD stability, energetic particle physics, transport and pedestal structure, boundary and divertor physics, RF heating, and scenarios and real-time control.

1. INTRODUCTION

The mission of the spherical tokamak NSTX-U [1] is to advance the physics basis and technical solutions required for optimizing the configuration of next-step steady-state tokamak fusion devices [2]. It will also support ITER and other critical fusion development needs enabled by its unique capabilities. NSTX-U will operate at up to 2 MA and 1 T for 5 seconds. 15 MW of neutral beam injection (NBI) power is available at different tangency radii, along with 6 MW of High Harmonic Fast Wave (HHFW) power. NSTX-U research is prioritized around three main objectives: to extend confinement and stability physics basis at low aspect ratio and high beta to lower collisionality towards burning plasma regimes; to develop operation at large bootstrap fraction and advance the physics basis for non-inductive, high-performance and low-disruptivity operation of steady-state compact fusion devices; and to develop and evaluate conventional and innovative power and particle handling techniques to optimize plasma exhaust in high performance scenarios. During the period of the NSTX-U Recovery Project (now in the construction and installation phase [3]) following operations in 2016 [4,5], there has been considerable analysis, theory and modelling progress in the areas of core MHD stability, energetic particle physics, transport and pedestal structure, boundary and divertor physics, RF heating, scenario optimization and real-time control, that will aid in achieving these objectives.

2. MACROSTABILITY AND 3D FIELDS

Global kink and tearing modes often limited performance in high-β NSTX plasmas, and also caused disruptions. To help identify stable operating regimes in NSTX-U, the resistive DCON (RDCON) code has been updated to calculate tearing mode stability (Δ′) in full toroidal geometry and benchmarked against MARS and PEST3 simulations [7,8]. Enabled by high numerical efficiency, RDCON is used to identify ranges in β_N and q_{95} that are stable to both n=1 external kink and 2/1 tearing modes. The Corsica equilibrium code [9] is used to vary the safety factor and pressure profiles. As an example, a model NSTX-U H-mode equilibrium at full field and high power (1.0 T, 2.0 MA, 12 MW NBI) is considered assuming a safety factor at the magnetic axis that is fixed just above unity. Fig. 1 shows the n=1 external kink can reach higher β_N at a few values of q_{95}, while Δ′ at the q=2 surface indicates the 2/1 tearing mode has a continuous (in β_N) window of stability at q_{95}~7-8. Taken together, the simulations for this example predict an operating window around q_{95}~7.5, with β_N~3 or possibly higher, that can be simultaneously stable to both modes. Additional scans will be used to more broadly guide NSTX-U operations to optimize high performance plasmas including ramp-up. The more tangential NBI in NSTX-U provides additional flexibility to access q_{min}>2 and optimize rotation profiles to further stabilize tearing modes.

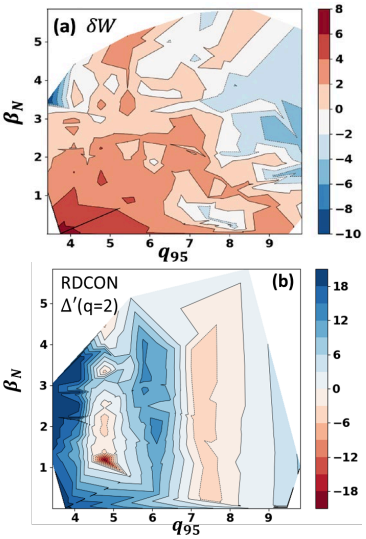

Fig. 1: (a) n=1 external kink stability (δW>0, stable) and (b) 2/1 tearing stability (Δ′<0, stable), as a function of q_{95} and β_n for a 2 MA, 1 T, 12 MW NSTX-U scenario (q_{min}→1⁺).

Extensive metrology and plasma response modeling with IPEC [10] and M3D-C1 [11] have been conducted to quantify the strength and sensitivity of the various sources of error fields on NSTX-U [12]. The modeling has been used to help inform tolerances on coil alignments in the NSTX-U Recovery Project by considering the effect of misalignments on resonant fields and on perturbations to the magnetic pitch on plasma facing components. The alignment tolerances of the PF coils near the outer midplane are found to be set by a constraint on the amplitude of the 2/1 resonant error field, while the tolerances of the PF coils near the divertor regions are found to be set by a constrain on the fractional perturbation of the magnetic field pitch at the divertor plates. Additional calculations show that misalignments in PF coils cause strike-point splitting and can extend divertor footprints. However, for expected error field amplitudes the strike point locations are contained within the divertor region designed to handle high heat fluxes [13].

Disruption mitigation simulations have been carried out for NSTX and NSTX-U equilibria using the M3D-C1 code to better understand how to optimize disruption mitigation in NSTX-U and other tokamaks. Using the recently incorporated KPRAD radiation model [14,15] and a wall model with realistic resistivity [16], simulations explore how the presence of impurities in vertically unstable plasmas. With large quantity of impurities, a rapid reduction in stored thermal energy is predicted, as well as the onset of stochastic magnetic fields due to non-axisymmetric MHD instabilities. While the current quench also occurs more rapidly, so does vertical displacement, with the result that a significant fraction of the plasma current remains when the plasma contacts the wall. Corresponding forces on the vessel (from both halo and eddy currents) are found to be

comparable in the cases with and without impurities. Future work will consider cases with even greater quantities of impurities, in order to quantify how short the current quench time must be in order to avoid having significant plasma current present when the plasma contacts the wall. An additional study explored the possibility of using an electromagnetic pellet injection (EPI) capability in NSTX-U. An EPI system could offer a fast response time and high enough pellet speed to deposit payloads in the plasma core [17]. To model this, M3D-C1 simulations were performed using a new pellet injection module [14] in which a single C-pellet was rapidly injected into an NSTX-U-like plasma using a carbon ablation model. Preliminary 2D simulations in NSTX-U suggest that the carbon content in a 1 mm radius carbon pellet (~3.2×10^{20} atoms) should be sufficient to mitigate the plasma if entirely ablated.

3. ENERGETIC PARTICLE PHYSICS

The phase-space-resolved reduced energetic particle (EP) transport *kick* model has been extended to include low-frequency, non-Alfvénic perturbations and validated against a variety of instabilities such as sawteeth, kink/fishbones and neoclassical tearing modes [18]. Recent analysis has further extended the application of the kick model to investigate the impact of the coupled n=1 kink + 2/1 tearing modes, commonly observed in NSTX plasmas, on fast ion transport [19]. The kink / tearing eigenmode structures, inferred from a synthetic diagnostic using forward modelling of soft x-ray measurements, are used to compute a kick probably matrix via ORBIT simulations. The fast ion loss and corresponding neutron rates are self-consistently predicted using TRANSP / NUBEAM with this kick probability matrix. Fig. 2(b) illustrates the relative difference in neutron rate between simulation and experiment as the kink / tearing mode amplitude increases (Fig. 2a). It is shown that the relative difference is ~10% when the modes are excluded. The difference is reduced when the kink / tearing modes are included, but only when they are treated as being phase-locked (as observed in experiment), as opposed to assuming uncorrelated randomly-phased modes as typically assumed for Alfvénic instabilities. Inspection of the simulations indicates a transport channel forms between the phase space islands of kink and tearing modes through which fast ions are transported from near the magnetic axis to the q=2/1 surface, and the sensitivity of this transport depends on the relative mode phasing. Additional simulations scaling the mode amplitudes show that the experimentally inferred island width (~7 cm) appears to be sitting just below the onset of very large fast ion loss caused by orbit stochasticization (Fig. 2c). This suggests that the tearing mode island growth may be limited due to the interaction with kink mode and fast ions. A kinetic fast-ion module for M3D-C1 has been recently developed to simulate the self-consistent interaction between (multiple) MHD modes and fast ion dynamics.

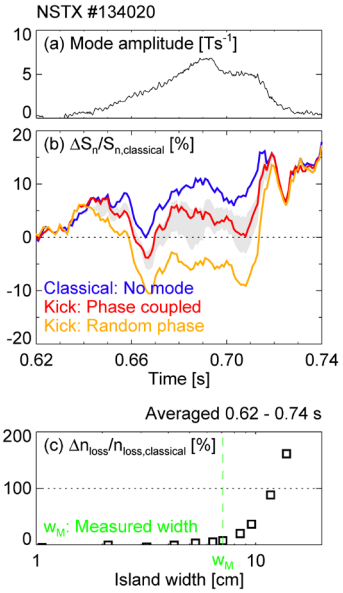

Fig. 2: (a) Measured amplitude of coupled n=1 kink + 2/1 tearing mode. (b) Relative difference in neutron rate between simulation and experiment, for classical losses only, or when including kick-model transport from the kink / tearing modes. (c) Predicted fast ion loss from phase-couple kink/tearing mode, for different tearing mode island widths. Reproduced from [19].

Chirping and avalanches are key fast ion loss mechanisms due to Alfvén eigenmodes (AEs). Previous analysis has indicated that AEs in NSTX often chirp as the high-beta, low-aspect ratio equilibrium sufficiently weaken ion-scale turbulence that can otherwise mediate a transition to the chirping behavior. Recent analyses have focused on understanding the nonlinear dynamics of chirping in NSTX(-U), using a guiding-center code (ORBIT) coupled with a delta-f formalism [20]. The simulations successfully reproduce observed chirping behavior (Fig. 3) with frequencies following the scaling predicted by adiabatic chirping theory, $\delta f = \pm(16\sqrt{2}/\pi^2 3\sqrt{3})\gamma_L\sqrt{\gamma_d t}$ [21]. The simulations indicate the onset of chirping can be triggered by a sudden increase in mode damping (γ_d), as can occur by the mode contacting the continuum. The sustainment of wave chirping is found to be associated with a sequence of amplitude crashes and local manipulation of the density gradients that maintain coherent holes and clumps in the distribution function that maintain an energy drive [22]. The simulations were also used to investigate the onset of more deleterious avalanches observed in NSTX with super-Alfvénic beams ($V_{beam}/V_A>1$, as expected for α-particles in burning plasmas like ITER). The avalanche onset requires multiple

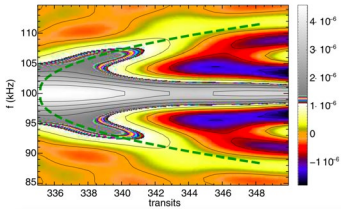

Fig. 3: (top) Evolution of chirping Alfven eigenmode frequency from ORBIT + delta-f simulations. Dashed line indicates theoretical scaling of adiabatic chirping. Reproduced from [20].

Alfvénic modes with sufficient resonance overlap. The simulations reproduce explosive growth of multiple modes for small changes in fast ion drive, indicating threshold-like behavior and the eventual inadequacy of the δf approach as wave-wave nonlinearities likely become important [23].

The presence of NBI-driven sub-cyclotron compressional (CAE) and global (GAE) Alfvén eigenmodes has previously been correlated with the core flattening of central T_e in high power NSTX discharges. Significant theoretical progress has been made in understanding the stability of these modes and identifying ways to stabilize them in order to test their impact on thermal confinement. Linear hybrid MHD/kinetic-fast-ion simulations (HYM) have been run for NSTX-like H-mode conditions [24] spanning a wide range of beam injection geometry, $\lambda_0 \approx (v_\perp/v)^2$, and velocity, v_0/v_A. Fig. 4(top) illustrates characteristic stability boundaries for three distinct types of modes: co- and counter-propagating GAEs, and co-propagating CAEs. In order to explain the simulated stability trends, a local analytic calculation of the fast ion drive was developed for an anisotropic beam distribution, including two-fluid dispersion and finite Larmor radius effects [25]. With additional approximations, simple instability conditions are derived which constrain the beam injection geometry and velocity required to destabilize each type of mode. E.g., sub-cyclotron cntr-propagating modes prefer more perpendicular beam injection, consistent with frequently observed cntr-propagating GAEs in NSTX (beam injection geometries λ_0~0.5-0.7). Co-propagating modes are more easily destabilized by tangential injection due to the different signs of $\partial f_{beam}/\partial(v_\parallel/v)$ which drive their respective resonances. With the more tangential beams in NSTX-U (λ_0~0.0) it may therefore be possible to stimulate co-propagating GAEs (at low field ~ large v_0/v_A) as a further validation of the theory. All types of modes have larger growth rates for larger values of v_0/v_A, but cntr-GAEs can be excited at smaller values than either co-GAEs or co-CAEs (co-GAEs require a larger Doppler shift to satisfy the resonance condition; co-CAEs have a weaker fast ion drive overall), also consistent with their prevalence in NSTX(-U) observations. Excellent agreement is found between the theoretically predicted range of unstable frequencies, the simulations results, and a large experimental database of NSTX observations, as shown in Fig. 4(bottom). Interestingly, the more tangential beams available in NSTX-U are predicted to have a stabilizing influence on cntr-propagating GAEs, as already observed [26] and reproduced in simulations [27]. This flexibility in beam injection geometry provides a mechanism by which to stabilize the modes and investigate their potential impact on core thermal transport. Recent simulations and experiments for conventional aspect ratio tokamaks suggests GAEs are present, and are also predicted to be unstable in ITER, although with much smaller growth rates and amplitudes than observed on NSTX [28].

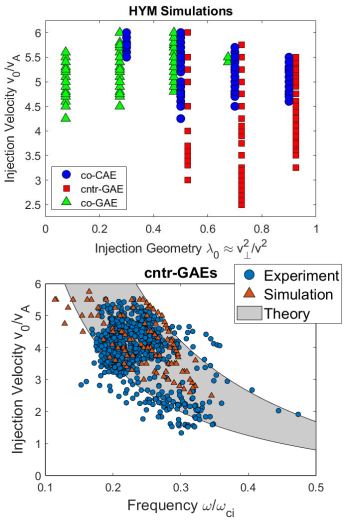

Fig. 4: (top) Unstable |n|=3-12 GAE/CAE modes predicted by HYM as a function of the beam injection geometry $\lambda_0 \approx (v_\perp/v)^2$ and normalized velocity v_0/v_A. (bottom) Comparison of experimentally observed counter-GAEs, unstable simulations, and theoretically predicted regimes, as a function of normalized injection velocity and frequency (ω/ω_{ci}). Reproduced from [24].

A large number of detailed ion cyclotron emission (ICE) observations in NSTX and NSTX-U plasmas have recently been summarized [29]. The measurements NSTX(-U) identify many harmonics (1^{st}-7^{th}), with frequencies that scale with field but not density, ruling out Alfvénic modes. A number of distinct variations are observed, e.g. short bursts (≤100 μs); longer, weaker bursts; or quasi-stationary states. The ICE frequency maps neither to the plasma edge, nor the magnetic axis as found on other tokamaks, and often appears correlated with a strong gradient in the density near the half-radius. No correlation between measured neutron rate and ICE amplitude is observed. While these observations challenge current theories, if understood, ICE could be considered for use as an additional α-particle relevant diagnostic for ITER and other burning plasmas.

4. TRANSPORT AND PEDESTAL STRUCTURE

Previous high-k scattering measurements and gyrokinetic simulations suggest electron-scale ETG turbulence is present in many NSTX discharges and may therefore contribute to anomalous electron thermal losses [30]. The observed fluctuation amplitudes qualitatively scale with many theoretical expectations, however the transport predicted by nonlinear gyrokinetic simulations does not always reproduce experiment [31]. To comprehensively validate ETG predictions, a novel synthetic diagnostic for high-k scattering has recently been developed to mimic the response function of the high-k scattering diagnostic [32]. Along with inferred energy fluxes, the measurements are used to constrain nonlinear GYRO simulations in a moderate-β NSTX H-mode where electromagnetic modes are not expected to play a significant role [33]. Numerous nonlinear parameter scans

were used to quantify the sensitivity of the predicted transport and high-k fluctuation spectra. Fig. 5 provides two examples of predicted synthetic high-k spectra (lines) compared to experiment (symbols) at a radius of r/a≈0.7. By varying input parameters within uncertainties, agreement is found in predicted transport, the high-k spectra shape (Fig. 5d), as well as the relative change in amplitude for two different discharge times where the local density gradient is changed, giving confidence that ETG can in fact fully account for the observed transport and fluctuations in this case at moderate β. These validated simulations can be used to qualify reduced ETG transport models. Additional local, ion scale simulations (GYRO) for this case illustrate the profile gradients sit just below the onset of very large, stiff ITG/TEM transport [34]. It is in these conditions (strong electron-scale drive, near-marginal ion-scales) that multi-scale effects have been found to be important in other tokamaks [35]. However, recent global ion-scale simulations (GTS) for this NSTX discharge predict that profile-shearing effects at the relatively large values of $\rho_* = \rho_s/a$ predict negligible ion-scale transport [36], consistent with the observation of neoclassical ion thermal transport, further supporting the dominance of electron-scale turbulence as the sole anomalous loss mechanism. A novel pseudolocal soft X-ray tomography diagnostic concept to measure electron-scale temperature fluctuations (δT_e) has been recently proposed [37]. Modeling indicates the method would be sensitive to ETG fluctuation amplitudes predicted above, and would provide an additional constraint more directly relevant to the ETG dynamics.

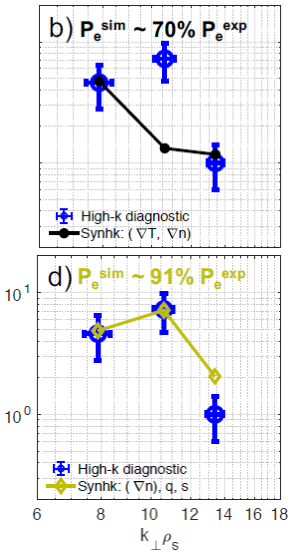

Fig. 5: Power spectra from high-k microwave scattering measurements (symbols) and ETG simulations + synthetic diagnostic (lines). Reproduced from [32].

A recently developed reduced model for microtearing mode (MTM) transport [38] has been tested against a variety of high-beta NSTX H-mode discharges [39]. The model makes improvements to older slab theory by treating arbitrary electron collisionality and including magnetic curvature effects. As a result, the model has been found to reproduce many of the linear gyrokinetic results predicted in NSTX discharges such as the variation of real frequency and growth rates with poloidal wavenumber (Fig. 6a), beta, collisionality, and electron temperature and density gradients. The model also solves a nonlinear dispersion relation to self-consistently determine a saturated magnetic fluctuation amplitude, $\delta B/B_0$, which also agrees with some of the nonlinear simulation predictions. Using this saturated amplitude with a Rechester-Rosenbluth like stochastic transport model provides the basis for the electron thermal transport model. The predicted T_e profiles using this model (in conjunction with the Multi-Mode Model within TRANSP) provides significantly improved agreement for a high collisionality NSTX H-mode discharge in (Fig 6b) as compared to predictions without the MTM model. However, the model overpredicts transport at low collisionality, in part due to the fact that the saturation model scales too weakly with collisionality (compared to nonlinear gyrokinetic simulations). The inability to reproduce the key scaling with collisionality motivates continued development of reduced transport models at high beta and low aspect ratio that enable more accurate predictions for high-performance scenarios.

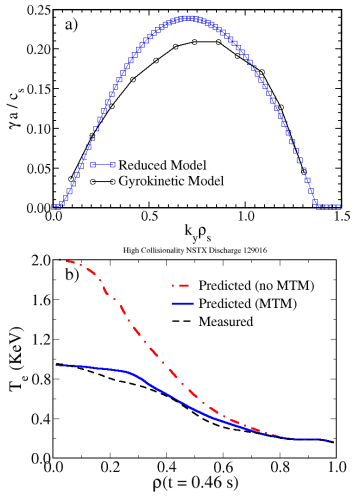

Fig. 6: (a) Linear MTM growth rates from gyrokinetic simulations and reduced model. (b) Experimental T_e profiles compared to predictions without and with MTM transport model . Reproduced from [39].

Previous observations have found that carbon impurity transport is often near neoclassical predictions especially in high-collisionality H-modes where ion thermal transport is also neoclassical, whereas deviations from neoclassical were noted at low collisionality [40]. This analysis has been recently extended as part of a multi-machine impurity transport validation study [41]. Considering a much larger database of discharges, carbon peaking (given by the local normalized gradients, $a/L_{n,C}$) at mid-radius is found to be robustly consistent with neoclassical predictions (NEO, including sonic rotation). However, significant deviations are observed farther out (r/a≥0.65). These deviations occur over a range of collisionality. Linear gyrokinetic analysis (CGYRO) indicates that microtearing modes are unstable for high ν_* (as typical for high-β NSTX H-modes), however they produce negligible impurity transport ($\Gamma_c \sim 0$). At lower ν_*, ballooning modes are found that predict carbon fluxes comparable in magnitude to the neoclassical predictions, but in the same direction and therefore also unable to explain the discrepancy. Further analysis is required to understand what mechanisms explain the carbon profiles in these regions.

The Enhanced Pedestal (EP) H-mode regime is an attractive ELM-free scenario for next-step Advanced Tokamak devices as it achieves $H_{98y,2}$ > 1.3 at large Greenwald density fraction (f_{GW} > 0.7), large bootstrap current fraction (f_{BS} > 0.7) and large plasma current compared to the toroidal field (I_p/B_T = 2 MA/T) [42]. EP H-mode occurs on NSTX when the edge ion collisionality becomes sufficiently small (ν_{i*} < 0.3) such that a modest reduction in the edge density leads to a large reduction in the dominant neoclassical ion energy transport in the pedestal [43]. This is demonstrated in Fig. 7, where EP H-mode operating points (red and orange squares) are compared to a wide-pedestal H-mode discharge (blue points) and contours derived from a large database of NSTX discharges. The y-axis is the maximum edge ion temperature gradient (∇T_i) and the x-axis represents the leading terms of neoclassical scaling measured at the location of the maximum ∇T_i. The dashed lines indicate the neoclassical scaling for constant local ion heat flux (q_i). The filled contours indicate the regime most often accessed where 83% of the database entries reside within the thick black contour. EP H-mode is a regime that achieved the largest edge ∇T_i at uniquely low edge collisionality that was facilitated by low edge density, often accessed transiently following a large ELM. Linear MHD (M3D-C1) and gyrokinetic (CGYRO) simulations demonstrate that the pedestal profiles are unstable to kink/peeling modes (Fig. 8a) and sitting within 10% of kinetic ballooning mode (KBM) pressure gradient thresholds, $\alpha \sim \nabla p$ (Fig. 8b), respectively. Measurements with beam emission spectroscopy (BES) show that in the EP H mode, fluctuations shift to higher frequency and become more directed in the ion-diamagnetic direction, consistent with MHD-like instabilities. The presence of these pressure and current-driven instabilities provides a mechanism for enhanced particle transport that can lock-in the new profiles at increased ∇T_i and lower the edge density, with improved energy confinement. Gyrokinetic analysis also predicts a number of other modes are unstable (MTM, ETG, TEM) that likely contribute to establishing the pedestal profiles as they evolve to the KBM and kink/peeling instability thresholds.

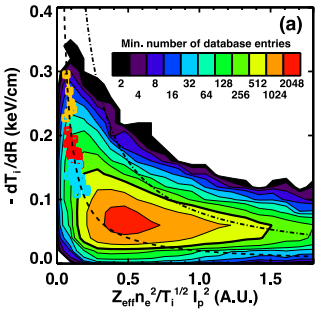

Fig. 7: (top). Database of maximum edge ∇T_i versus leading order terms of neoclassical transport. Dashed lines represent fixed $q_{i,neo}$.

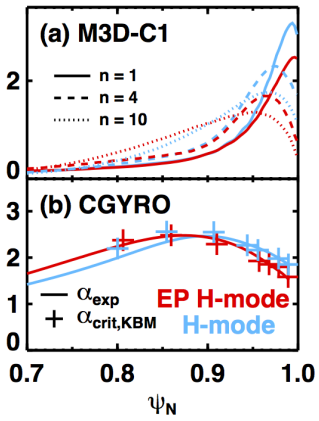

Fig. 8. (a) MHD kink/peeling eigenfunctions (M3D-C1), and (b) normalized pressure gradient, α, from experiment (lines) and KBM thresholds (CGYRO, symbols) for both H and EPH mode. Reproduced from [43].

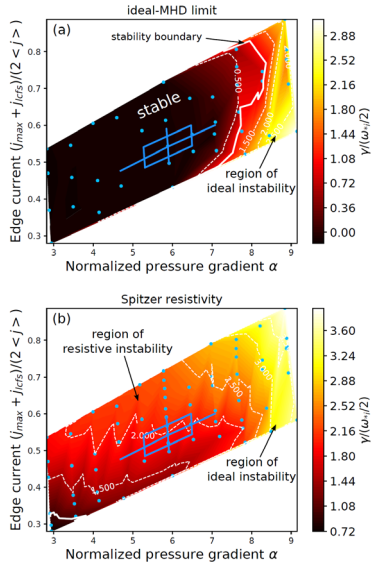

Fig. 9: Normalized peeling-ballooning mode growth rates vs. normalized pedestal pressure gradient, α, and current density j, for (a) ideal, and (b) resistive MHD simulations (M3D-C1). Experimental values shown by cross-hairs. Reproduced from [46].

Previous MHD stability calculations for fully-developed NSTX ELMy H-modes predict pedestals are weakly unstable to ideal peeling-ballooning (P-B) modes, with growth rates normalized to half the ion-diamagnetic freqeuncy $\gamma/(\omega_{*i}/2) \leq 0.1$ [44,45], about ten times smaller than that predicted at conventional aspect ratio. Recent MHD simulations (M3D-C1) have been run to quantify the impact of various non-ideal effects [46]. An example is shown in Fig. 9 for a highly-shaped ELMy H-mode, where normalized growth rates (maximized over toroidal mode numbers n=1-20) are computed for a range of self-consistent global equilibria that vary normalized pedestal pressure gradient and current density. Fig. 9a illustrates that the experiment sits firmly in the range of stable ideal P-B modes. However, the modes become much more unstable when including Spitzer resistivity, and the unstable boundary moves to much lower edge current and pressure gradient (Fig. 9b). In the resistive limit, normalized growth rates for the experiment correspond to $\gamma/(\omega_{*i}/2) \sim 2$ indicating the resistive P-B modes are expected to be unstable, consistent with the ELMy H-mode regime. Similar simulations in DIII-D show resistivity has a much weaker effect, likely due to higher pedestal temperature (lower resistivity). Work towards a generalized pedestal structure model, including resistive MHD P-B stability and gyrokinetic KBM stability, is commencing and will be tested in NSTX-U to clarify the role of resistivity on establishing ELMy H-mode pedestal structure.

Deuterium atomic density n_D profiles were measured, and upper

estimates of ionization rates inferred, on the LFS midplane of NSTX-U to enable fueling and pedestal transport studies [47]. Deuterium atomic densities are calculated by inverting the line-integrated D_α brightness measured by the 2D edge neutral density diagnostic (ENDD) camera. Ionization rates are obtained using atomic rate coefficients inferred using local n_e and T_e profiles, although they represent an upper estimate as the molecular contribution to D_α emissivity has been neglected. The assumptions used in the n_D and ionization rate derivations were validated using the Monte Carlo neutral transport code DEGAS 2. Good agreement in D_α emissivity profiles is found over a database of NSTX-U L- and H-modes, although far-SOL emission was under predicted possibly related to intermittent transport and uncertainties in molecular rates. The combined ENDD/DEGAS 2 analysis can generate n_D and n_{D2} radial profiles, extending the direct ENDD measurements in the core and SOL where emission is either too weak or dominated by molecular processes. Narrower n_D profiles are observed inside the separatrix in H-mode discharges. During the pedestal build up, an increase in peak ionization rate is observed with no significant change in either the pedestal or the ionization rate width (Fig. 10).

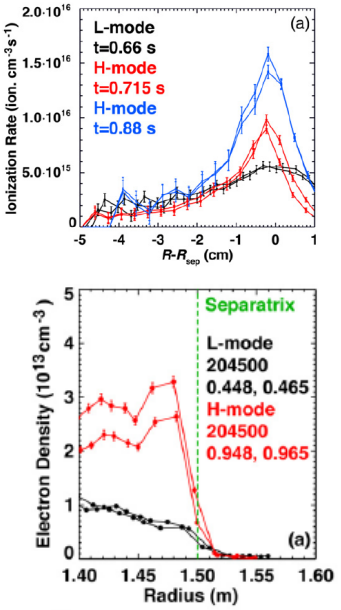

Fig. 10. (top) Measured ionization rates (upper-estimate) and (b) electron density profile in the edge of L- and H-mode phases of NSTX-U discharge. Reproduced from

5. BOUNDARY AND PMI

Detailed scrape-off-layer (SOL) turbulence measurements using gas puff imaging (GPI) [48] have been used to study dynamics associated with the L-H transition, ELM onset, inter-ELM turbulence, and divertor fluctuations. Understanding these phenomena is critical for understanding access to, and performance of, the H-mode pedestal, as well as the SOL heat flux width and corresponding divertor target peak heat fluxes that constrain plasma exhaust solutions and material choices in reactor conditions. Analysis and observations probe velocity dynamics prior to L-H transition [49], the appearance of "wakes" following the filamentary dynamics observed in the inter-ELM period of H-mode plasmas [50], and correlations between global core MHD events and SOL filaments [51]. Two additional examples are highlighted here.

First, the characteristic behavior of SOL filaments observed before, during and after ELM crashes was analyzed exploiting the high temporal (2.5 μs) and spatial resolution (10 mm) of the GPI system [52]. A database of 159 ELM events (including type I, III and V ELMs) was generated from the 2010 NSTX measurement campaign. Data analysis methods were applied to estimate the number of filaments as well as their velocities, sizes, and distance from the separatrix. The distribution functions of each parameter were computed as a function of time relative to ELM onset ($t-t_{ELM}$), and the characteristic behavior of the ELM filament was determined from the evolution of the median of each distribution function. The analysis reveals that during the increased filamentary activity prior to the ELM crash, multiple filaments coalesce into a single, circular ELM filament structure that propagates outwards. Surprisingly, the radial velocity of the ELM filament increases ~linearly with distance from the separatrix in the ~25 μs preceding the ELM crash (Fig. 11). This exponential acceleration ($V_{rad} = dr/dt \sim r$) of a single filament immediately prior to the ELM crash has never been observed. Following the ELM crash, which lasts for a median time of 100 μs, the radial velocities settle back to the pre-ELM level. The current-filament model [53], in which the filament is modelled as a current carrying wire, can explain coalescence of filaments, their circular shape, and the poloidal acceleration. It also predicts a repulsive force from the current hole forming in the plasma during the ELM crash that would cause radial acceleration However, it cannot reproduce the exponential acceleration. A possible explanation could be that reconnecting edge structures (plasmoids) emerge during the nonlinear dynamics of ELM filaments and contribute to current transport in the SOL [54].

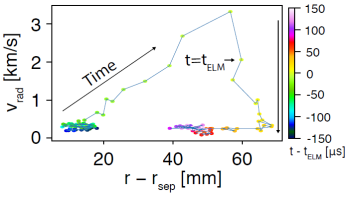

Fig. 11. ELM filament radial velocity vs. distance from separatrix. The time-to-ELM crash is given by the colorbar. Reproduced from [52].

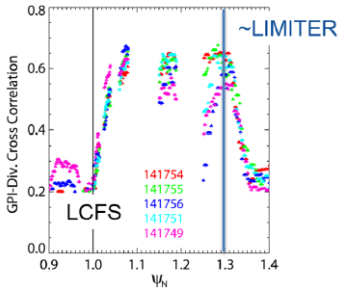

Fig. 12. Maximum cross-correlation between upstream (GPI) and divertor target (Li I emission) fluctuations, plotted vs. ψ_N. Reproduced from [55].

Second, the correlation between divertor fluctuations and upstream turbulence (GPI) was studied in NSTX ohmic L-mode discharges [55]. The divertor target fluctuations were measured using a fast camera filtered for Li I emission, which localizes the observations to within a few mm of the divertor plate due to the short ionization mean free path. Divertor radial turbulence scale lengths as well as radial and poloidal turbulence propagation velocities are comparable to those on the low field side (LFS) midplane as measured by GPI. For each divertor radial location, the maximum cross correlation with every pixel in the GPI view was evaluated. The midplane/divertor correlation as a function of normalized poloidal flux for the five discharges is shown in Fig. 12. Large correlations, up to 0.7, are observed in the far SOL. Approaching the separatrix (ψ_N<1.08), divertor fluctuation levels and radial correlation lengths gradually decrease, as does the correlation between midplane and divertor turbulence. The reduction in correlation is consistent with that predicted in the electrostatic two-region blob model (56) due to X-point geometry and collisionality. A measured reduction in turbulence radial velocity is also expected from the two-region model, due to a reduction in the effective resistivity of the blob circuit, which could influence the SOL heat flux width.

The various SOL turbulence observations provide some qualitative agreement with theory. However, the presence of strong amplitude intermittent filaments crossing from closed to open field lines, the possible role of electromagnetic effects (reconnection, drift-Alfvén dynamics), and the varying connection from upstream to divertor target drives the continued development of simulation capabilities.

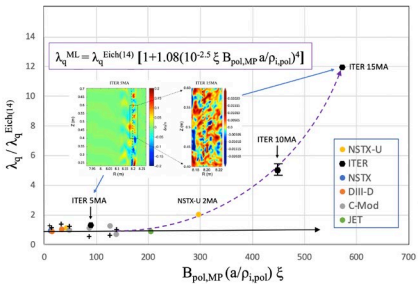

Fig. 13. Predicted heat-flux width deviation (XGC1), as a ratio of the empirical scaling. Line shows new fit derived from simulations. Reproduced from [58].

Recent total-f gyrokinetic simulations (XGC [57]) have reproduced empirical and theoretical scalings of the SOL divertor heat-load width λ_q in NSTX, DIII-D, C-Mod, JET, and the 5MA ITER H-mode plasmas, in the attached divertor condition. However, significantly enhanced widths are projected for ITER 10MA and 15MA plasmas. Similar excursions are predicted for NSTX-U full-current 2MA discharges (Fig. 13), but not for lower current (1.5 MA) [58]. The larger heat-flux widths are predicted due to the onset of collisionless trapped electron mode (TEM) turbulence across the magnetic separatrix that exhibit streamer-like eddies as opposed to more blob-like turbulence (see insets in Fig. 13). The TEM turbulence is enhanced by reduced collisionality and either weakened E×B shearing rate at small ρ_{i*} (for ITER) or large trapped particle fraction (at low-A in NSTX-U). A supervised machine learning program has been used to find a unified formula from all simulation and experimental λ_q data that includes dependencies on ρ_{i*}, collisionality, and inverse aspect ratio (Eq. in Fig. 13, where ξ=1+ 2.3Θ[(a/R$_0$)$^{1/2}$/ν_{e*} -1.75], and Θ is the heavy-side function). The NSTX-U simulations with enhanced λ_q predict a co-existence of streamers and blobs, which provide an experimental opportunity to validate key physics for ITER.

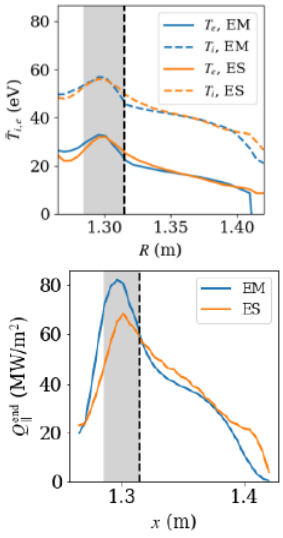

Fig. 14. Upstream temperatures and target heat fluxes predicted from EM simulations for NSTX-like model SOL (Gkeyll). Reproduced from [59].

The possible role of electromagnetic (EM) effects in scrape-off-layer simulations is now also being explored. First electromagnetic nonlinear full-f gyrokinetic simulations of turbulence on open field lines have been conducted using the GKEYLL code [59,60]. A model NSTX scrape-off-layer region has been simulated using a helical, open-field-line flux-tube with field-lines intersecting metal divertor plates on either ends. Changes in upstream midplane gradients and target fluxes are predicted when including EM effects for sufficiently large heating and fueling source rates (Fig. 14). The simulations also predict intermittent blob-like dynamics that can be statistically characterized and compared to experiment. Closed flux surfaces, shaping and X-point geometry are now being included to more realistically model the pedestal-SOL-wall dynamics.

Newly designed PFCs in the high heat flux regions of NSTX-U divertor tiles have a castellated design, in which narrow slices are cut into the graphite surface to eliminate transverse conduction. This reduces thermal stresses so that the PFCs are instead limited by surface temperature (graphite sublimation at T~1600° C). The Heat flux Engineering Analysis Toolkit (HEAT) has been developed and applied to predict surface heat flux and temperature as a function of plasma shaping and PFC geometry by coupling magnetic equilibrium, 3D CAD, SOL physics, and finite-volume solvers [61]. Fig. 15 illustrates a prediction of the 3D heat flux footprint in the lower divertor of a full-field,

highly-shaped NSTX-U projected scenario (1.0T, 2.0 MA), where variations due to the castellations (and fishscaling) are apparent. Without mitigation, sublimation limits can be reached within ~2.5 seconds at high power (10 MW). With the capability to simulate time varying discharges, additional HEAT analysis was used to predict the efficacy of strike-point sweeping on limiting PFC temperature rise. Fig. 15(bottom) shows that when the strike-point sweep frequency approaches 10 Hz, the sublimation limit is delayed until nearly 4 seconds and maximum temperatures are much smaller. Additional modules are being developed to incorporate SOL plasma radiation (and ELM loads) to predict PFC operational limits in additional scenarios employing radiative/detached divertors via impurity seeding.

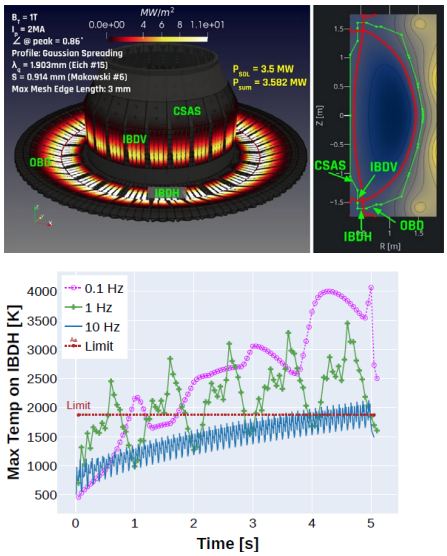

Fig. 15. (top) Predicted 3D target heat flux (HEAT) for a full-field NSTX-U projection. (Bottom) Predicted evolution of maximum PFC temperature for different strike-point sweep frequencies. Reproduced from [61].

As target heat fluxes in some high-power NSTX-U scenarios are predicted to reach values far exceeding solid material steady-state limits (as expected in reactor conditions), a number of novel liquid and evaporative lithium PFC solutions have been proposed for testing in future NSTX-U campaigns [62]. Previous modelling of one such concept, the lithium vapor box [63], has shown its feasibility in reducing target heat fluxes while maintaining a naturally stable detachment front due to the gradient in lithium vapor enabled by differentially pumping. Recent modelling has investigated the impact of additional deuterium puffing on controlling upstream lithium density [64]. SOLPS-ITER simulations based on an NSTX-U experiment (with an open divertor configuration) predict that upstream lithium concentration can be kept to $n_{Li}/n_e<2\%$ with sufficient D_2 puffing in the private flux region, while maintaining reduced target temperatures and heat fluxes in detached conditions. Future simulations will investigate the effect of divertor closure and drifts in for possible future NSTX-U lithium vapor box concepts.

6. RF PHYSICS

NSTX-U is equipped with a 12-strap high harmonic fast wave (HHFW) antenna, with up to 6 MW (30 MHz) for heating and current drive that was used on NSTX to study electron thermal transport, rotation, and energetic particle physics. In many experiments, however, a large amount of HHFW power was observed to be missing from the plasma core, correlated with the presence of bright plasma spirals in the SOL from the antenna to the divertor regions. Previous full-wave modelling suggested this is due to losses in the SOL from cavity modes. More recent modelling, using 2D full-wave simulations (FW2D) adapted to include realistic vessel boundary shapes, has been used to further investigate the sensitivity of these losses to antenna phasing, SOL density and magnetic field strength [65]. The simulations predict that SOL losses should be reduced for larger antenna phasing and smaller lower density in front of the antenna (Fig. 16), consistent with experimental observations and previous AORSA 2D simulations [66]. Generally it is found that losses are minimized as the antenna density approaches and drops below the fast wave cutoff density (red squares). Predicted SOL losses are further minimized for smaller distance between the LCFS and antenna, Δ_{SOL} (smaller SOL volume) and larger magnetic field, providing a route to optimization in NSTX-U.

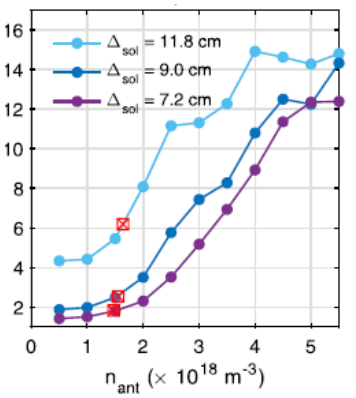

Fig. 16. Predicted SOL power loss (% of HHFW injected power) vs. density in front of the antenna (n_{ant}) and gap between LCFS and antenna (Δ_{SOL}). Reproduced from [65].

In addition to SOL losses, the absorption of HHFW heating in the presence of NBI was observed in NSTX to be weaker than in conditions without NBI, especially to electrons. Additional 2D full-wave simulations (AORSA, using rectangular boundaries) were used to predict the competition between electron and fast ion absorption in NSTX-U without and with NBI [67]. Assuming a Maxwellian distribution of fast ions with a temperature proportional to the effective energy computed by TRANSP/NUBEAM, the simulations predict larger absorption to electrons

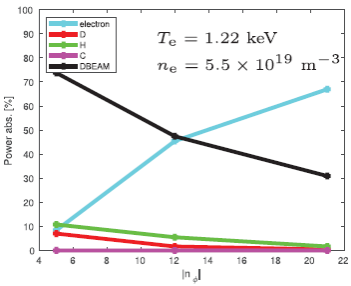

Fig. 17. HHFW absorbed power vs. antenna phasing, assuming 2% H in a full field NSTX-U projection. Reproduced from [67].

can be achieved when going to larger field and larger antenna phasing (~toroidal mode number, Fig. 17). The electron absorption is also increased for larger ratios of T_e/T_i (with or without NBI) which can not *a priori* be predicted without more accurate transport models. The above simulations assumed a 2% hydrogen concentration based on NSTX results, which has marginal impact on absorption in simulations above (green line, Fig. 17). However, additional simulations at larger concentration (up to 10% H) predict more significant hydrogen absorption due to the presence of the 2nd H harmonic in the core, indicating a new possible operating regime that may be relevant to ICRH in ITER.

The various 2D simulations above provide considerable insight into how to manipulate HHFW antenna phasing, magnetic field, plasma density, and SOL geometry to minimize SOL losses and optimize thermal coupling, especially in the presence of NBI. To provide more realistic, self-consistent prediction of these effects, a state-of-the-art generic electromagnetic simulation tool for modeling RF wave propagation, Petra-M, has been developed [68,69]. The Petra-M framework solves Maxwell's equations in the frequency domain using realistic 3D CAD drawings of HHFW antenna geometry, vacuum vessel, and internal passive plates. Fig. 18 shows the predicted HHFW 3D electric field in a model NSTX-U scenario (using an anisotropic cold plasma model in the torus with artificial collisions), where the toroidal propagation due to high antenna phasing is apparent. Additional simulations at lower antenna phasing predict much stronger interactions in the SOL, consistent with the NSTX experimental observations. With these stronger SOL interactions at low antenna phasing, the 3D simulations also predict stronger electric fields on the internal passive plates which will be important to consider for understanding impurity generation and RF sheath effects.

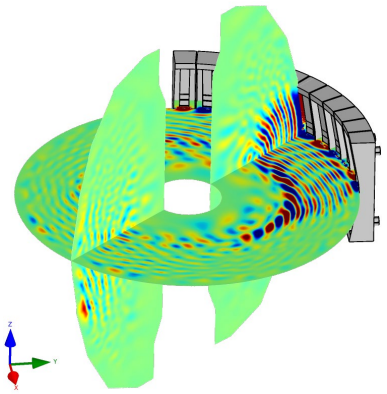

Fig. 18. Predicted HHFW 3D wave field (Petra-M). Reproduced from [68].

7. SCENARIO OPTIMIZATION AND CONTROL

To facilitate efficient exploration of NSTX-U operating space, multiple approaches for optimizing steady-state scenario and actuator trajectories using integrated-model-based prediction have been recently developed. Using integrated predictive TRANSP simulations, an automated iterative approach has been developed and used to optimize non-inductive ramp-up in high-performance scenario projections [70]. This approach identified a slightly improved solution with respect to the original optimization performed manually. To accelerate the iterative optimization, reduced models have been proposed and implemented for current profile evolution [71] and momentum transport [72]. Machine learning neural-net approaches have also been developed to generate very rapid models for neutral beam heating, torque and current drive profiles based on a database of NUBEAM calculations [73]. A similar neural-net based model for predicting the shape of electron density and temperature profiles was developed based on a database of experimental profiles [74]. Using these machine-learning accelerated approaches, optimization of steady-state scenarios and actuator trajectories has been demonstrated with convergence achieved in minutes as compared to several days [75]. Future work will focus on expanding and validating the predictive capability of the machine learning models.

While the actuator trajectories designed above provide guidance on achieving optimal performance, real-time feedback control algorithms and measurements are also required to reliably achieve and maintain desired stable plasma conditions. For high power NSTX-U discharges, it is expected that heat flux mitigation strategies will be needed, including control of flux expansion. To facilitate this, an algorithm for identifying and controlling the snowflake diverter configuration was developed [76]. The model-based control algorithm enables multi-input multi-output control over the diverter coils to track operator specified snowflake diverter characteristics. In addition to shape control, a reduced-model-based feedback control of the safety factor profile was developed [77] and tested using the recently improved TRANSP closed-loop control modelling [78]. To enable fast profile measurements suitable for real-time applications, a scalable framework for Thomson scattering analysis was established using high speed analog digital convertors, a dedicated real-time server, and new analysis software optimized for fast and accurate fitting of the Thomson spectra [79]. With these improvements, electron density and temperatures can be computed with <17 ms latency with accuracy that matches the slower post-shot analysis.

A reduced semi-empirical model using time-dependent axisymmetric vacuum field calculations has been developed to determine optimal prefill and feed-forward coil current targets required for reliable direct induction startup on NSTX-U and MAST-U [80]. The model has recently been used to help MAST-U achieve first plasma

[81]. 3D resistive MHD simulations (NIMROD) of coaxial helicity injection based on NSTX experiments predict non-inductive current generation from plasmoid-mediated reconnection scales favorably to higher B_T [82]. While there are no current plans for CHI in NSTX-U, the favorable scaling implies that it may still be an effective approach for non-inductive startup in future devices operating at higher field. initiate

8. SUMMARY

Considerable progress has been made in validating the mechanisms responsible for core thermal transport, fast ion transport, and H-mode pedestal structure, to improve understanding of confinement scaling and achievable performance limits at low-aspect ratio. Improved modeling of global MHD and energetic particle instabilities, as well as developments in integrated predictive modeling and realtime control methods, provide tools to help optimize scenarios in future NSTX-U experiment. Numerous observations of scrape-off-layer (SOL) and divertor turbulence have provided detailed measurements of dynamics that influence L/H transition, ELM onset, inter-ELM turbulence, and SOL-divertor connection. New simulation and modeling capabilities have been developed to predict boundary turbulence, which influences particle and heat loads to divertor targets, and to predict operational limits of plasma facing components. The recent progress in analysis, simulation and modeling of NSTX and NSTX-U helps advance the physics basis and technical solutions required for optimizing the configuration of next-step steady-state tokamak fusion devices.

ACKNOWLEDGEMENTS

This research was supported by U.S. DOE Contracts DE-AC02-09CH11466, DE-FG02-02ER54678

REFERENCES

[1] J.E. Menard et al., Nucl. Fusion **52**, 083015 (2012).
[2] J.E. Menard et al., Nucl. Fusion **51**, 103014 (2011); **56,** 106023 (2016); Phil. Trans. R. Soc. A **377**, 20170440 (2019).
[3] S.P. Gerhardt et al., IAEA-FEC TECH/P3-17 (2021).
[4] J.E. Menard et al., Nucl. Fusion **57**, 102006 (2017).
[5] S.M. Kaye et al., Nucl. Fusion **59**, 112007 (2019).
[6] J.E. Menard et al., IAEA FEC TECH/2-4 (2021).
[7] Z.R. Wang et al., Phys. Plasmas **27**, 122503 (2020).
[8] A.H. Glasser et al., Phys. Plasmas **23**, 112506 (2016).
[9] S.H. Kim et al., Nucl. Fusion **56**, 126002 (2016).
[10] Park J.-K., Boozer A.H. and Glasser A.H. Phys. Plasmas **14** 052110 (2007).
[11] N.M. Ferraro. Phys. of Plasmas **19**, 056105 (2012).
[12] N.M. Ferraro et al., Nucl. Fusion **59** 086021 (2019).
[13] S. Munaretto et al., Nucl. Fusion **59** 076039 (2019).
[14] B. Lyons et al., Plasma Phys. and Contr. Fusion **61**, 064001 (2019).
[15] N. Ferraro et al., Nucl. Fusion **59**, 016001 (2019).
[16] N. Ferraro, et al., Phys. Plasmas **23**, 056114 (2016).
[17] R. Raman et al., Nucl. Fusion **59**, 016021 (2019).; IAE FEC TECH/P5-17 (2021).
[18] M. Podesta et al., Nucl. Fusion **59**, 106013 (2019); IAEA FEC TH/P1-26 (2021).
[19] J. Yang et al., Plasma. Phys. Control Fusion **64**, 045003 (2021).
[20] R.B. White et al, *Phys. Plasmas* **26**, 092103 (2019); IAEA FEC TH/P1-13 (2021).
[21] H. L. Berk et al., Phys. Lett. A **234**, 213 (1997).
[22] R. B. White et al., *Phys. Plasmas* **27**, 052108 (2020).
[23] R. B. White et al., *Phys. Plasmas* **27**, 022117 (2020).
[24] J.B. Lestz et al., Nucl. Fusion, in press (2021). https://doi.org/10.1088/1741-4326/abf028
[25] J.B. Lestz et al., Phys. Plasmas **27**, 022513 (2020); Phys. Plasmas **27**, 022512 (2020).
[26] E. Fredrickson et al., Phys. Rev. Lett **118**, 265001 (2017). Nucl. Fusion **58**, 082022 (2018).
[27] E. Belova et al., Phys. Plasmas **26**, 092507 (2019).
[28] E. Belova et al., IAEA FEC TH/P1-27 (2021).
[29] E. Fredrickson et al., Phys. Plasmas **26, 032111 (**2019); IAEA FEC EX/P7-6 (2021).
[30] Y. Ren et al., Nucl. Fusion **57**, 072002 (2017); Nucl. Fusion **59**, 096045 (2019).
[31] W. Guttenfelder et al., Nucl. Fusion **53**, 093022 (2013).
[32] J. Ruiz-Ruiz et al., Plasma Phys. Control Fusion **62**, 075001 (2020).
[33] J. Ruiz-Ruiz et al., Phys. Plasmas **22** 122501 (2015); Plasma Phys. Control Fusion **61**, 115015 (2019).
[34] J. Ruiz-Ruiz et al., Phys. Plasmas **27**, 122505 (2020).
[35] N.T. Howard et al., Phys. Plasmas **23**, 056109 (2016).
[36] Y. Ren et al., Nucl. Fusion **60**, 026005 (2020).
[37] X. Chen et al., Rev. Sci. Instrum, in review (2021).
[38] T. Rafiq et al., Phys. Plasmas **23**, 062507 (2016).
[39] T. Rafiq et al., Phys. Plasmas **28**, 022504 (2021).

[40] F. Scotti et al., Nucl. Fusion **53**, 083001 (2013).
[41] N. Howard et al., IAEA FEC PD/1-1
[42] R. Maingi et al., Phys. Rev. Lett. 103, 075001 (2009).; S. Gerhardt et al., Nucl. Fusion **54**, 083021 (2014);
[43] D.J. Battaglia et al., Phys. Plasmas **27**, 072511 (2020).
[44] D. P. Boyle et al., Plasma Phys Control Fusion 53, 105011 (2011); A. Sontag et al., Nuclear Fusion 51, 103022 (2011).
[45] A. Diallo et al., Nuclear Fusion 51, 103031 (2011); Nuclear Fusion 53, 093026 (2013).
[46] A. Kleiner et al., Nucl. Fusion, in press (2021). https://doi.org/10.1088/1741-4326/abf416
[47] F. Scotti et al., Nucl. Fusion **61**, 036002 (2021).
[48] S. Zweben et al., Nucl. Fusion **55**, 093035 (2015).
[49] S. Zweben et al., Phys. Plasmas 28, 032304 (2021).
[50] S. Zweben et al., Phys. Plasmas 26, 072502 (2019).
[51] S. Zweben et al., Phys. Plasmas 27, 052505 (2020).
[52] M. Lampert et al., Phys. Plasmas 28, 022304 (2021).
[53] J. Myra, Phys. Plasmas **14**, 102314 (2007).
[54] F. Ebrahimi, Phys. Plasmas **24**, 056119 (2017).
[55] F. Scotti et al., Nucl. Fusion 60, 026004 (2020).
[56] J. Myra et al., Phys. Plasmas **13**, 112502 (2006).
[57] C.S. Chang et al., Nucl. Fusion 57, 116023 (2017).
[58] C.S. Chang et al. Phys. Plasmas 28, 022501 (2021); IAEA FEC TH/P4-4 (2021).
[59] N. Mandell et al., J. Plasma Physics 86, 905860109 (2020). Ph.D. Thesis, Princeton University (2021).
[60] A.H. Hakim et al., Phys. Plasmas 27, 042304 (2020)., IAEA FEC TH/3-4 (2021).
[61] T. Looby et al., in review (2021).
[62] M. Ono et al., IAEA FEC TECH/P7-11 (2021).
[63] R.J. Goldston et al., Phys. Scr. T167 014017 (2016); E. Emdee et al., Nucl. Mat. & Energy **19**, 244 (2019).
[64] E. Emdee et al., in review (2021).
[65] E.-H. Kim et al., Phys. Plasmas 26, 062501 (2019).
[66] N. Bertelli et al, Nucl. Fusion **54** 083004 (2014).
[67] N. Bertelli et al., Nucl. Fusion **59** 086006 (2019).
[68] S. Shiraiwa et al., EPJ Web of Conferences 157, 03048 (2017); IAEA FEC TH/7-2 (2021).
[69] N. Bertelli et al., IAEA FEC TH/P2-16 (2021).
[70] W.P. Wehner et al., Fusion Eng. and Design **146** 547 (2019).
[71] Z.O. Ilhan et al., Fusion Eng. and Design **123**, 564 (2017).
[72] I.R. Goumiri et al., Phys. Plasmas **24**, 056101 (2017).
[73] M.D. Boyer et al, Nucl. Fusion 59 056008 (2019).
[74] M.D. Boyer et al., Nucl. Fusion **61**, 046024 (2021).
[75] M.D. Boyer et al., IAEA FEC EX/P7-5 (2021).
[76] P.J. Vail et al., Plasma Phys. Control. Fusion **61**, 035005 (2019).
[77] Z.O. Ilhan et al., Fusion Eng. and Design **146** 555 (2019).
[78] M.D. Boyer et al, Nucl. Fusion **60** 096007 (2020).
[79] F. Laggner et al., Rev. Sci. Instrum 90, 043501 (2019).
[80] D.J. Battaglia et al., Nucl. Fusion **59**, 126016 (2019).
[81] J. Harrison et al., IAEA FEC P6 (2021).
[82] F. Ebrahimi, Phys. Plasmas **26**, 092502 (2019)